Author(s): Geng, Zhuoran; Laakko, Timo; Hokkanen, Ari; Södergård, Caj; Maasilta, Ilari; Mohammadi, Pezhman

Title: Material engineering and application of hybrid biomimetic-de novo designed elastin-like polypeptides

Year: 2024

Version: Published version

Geng, Z., Laakko, T., Hokkanen, A., Södergård, C., Maasilta, I., & Mohammadi, P. (2024). Material engineering and application of hybrid biomimetic-de novo designed elastin-like polypeptides. Communications Materials, 5, Article 152. https://doi.org/10.1038/s43246-024-00597-y

communications materials

Article

https://doi.org/10.1038/s43246-024-00597-y

Material engineering and application of hybrid biomimetic-de novo designed elastin-like polypeptides

Zhuoran Geng [1,3], Timo Laakko [2,3], Ari Hokkanen [2,3], Caj Södergård[2], Ilari Maasilta [1] & Pezhman Mohammadi [2]

The global concern over environmental consequences of petrochemical-derived plastics underscores the urgent need for sustainable and biodegradable polymers. In this context, elastin-like polypeptides emerge as a promising solution, offering multiple advantages, including remarkable mechanical properties, biocompatibility, customizable functionalities, and renewable sourcing through biosynthetic production in microbes, making them a compelling choice for various applications. We previously demonstrated accelerated engineering of a new class of elastin-like polypeptide-based materials through hybrid biomimetic-de novo predictive molecular design. The resulting variants exhibited enhanced molecular stability compared to their natural counterparts, catering to a range of technical applications that involve harsh downstream processing conditions. Here, we showcase the use of some of these previously discovered hybrid variants and illustrate the effective translation of the predicted molecular designs in structural and functional materials in several high-added-value applications. This includes multiscale drug-encapsulating vehicles with controlled release, multifunctional wound coverings, and all-aqueous-based biobased photoresists for creating 2D/3D microstructures.

The global concerns over the environmental impact of petrochemical-derived plastics have grown exponentially[1,2]. The widespread utilization of traditional plastics has resulted in ecological catastrophes, necessitating a shift towards more sustainable and biodegradable polymer alternatives[3,4]. Our present pursuit lies in the need for materials that can reduce ecological footprints while maintaining material performance and even surpass the demanding criteria set by their petrochemical-derived counterparts[3].

In recent years, taking inspiration from high-performance protein-based structural biomaterials such as silk, elastin, and resilin has led to the development of advanced functional materials[5–9]. Tropoelastin is the soluble precursor of elastin, an essential extracellular matrix protein that imparts elasticity and resilience to tissues such as skin, lungs, and blood vessels. It consists of alternating hydrophobic and hydrophilic domains, allowing it to self-assemble into extensible networks that provide mechanical strength and flexibility to connective tissues. Inspired by the repetitive sequences in tropoelastin, Elastin-Like Polypeptides (ELPs) are synthetic biopolymers characterized by the pentapeptide repeat sequence (VPGXG)n, where "V" is valine, "P" is proline, "G" is glycine, and "X" is a variable amino acid. ELPs mimic the properties of natural elastin, including reversible phase transitions in response to environmental changes such as temperature, pH, and ionic strength. ELPs exhibit a fascinating blend of physicochemical properties. ELPs inherit the remarkable mechanical properties of elastin, granting them a notable advantage over traditional plastics with customizable functionalities[5–9]. The high resilience, elastic behavior, and overall toughness are properties that are invaluable in applications demanding material durability and longevity. Additionally, ELPs exhibit a multifaceted suite of biocompatibility and biodegradability, which is pivotal in many medical and biological contexts, from drug delivery systems to scaffolds in tissue engineering, leveraging their ability to form diverse nanostructures and hydrogels for advanced therapeutic and diagnostic solutions. ELPs form a foundational platform in biomaterials engineering, driving innovations in medicine and biotechnology. The other major benefit lies in the renewable sourcing of ELPs, facilitated through their biosynthetic production in microbial systems via biotechnological methods[9].

Previously we demonstrated an AI-empowered material scientist (AIMS) predictive design workflow for arbitrary sequences with α-helical conformation as guest motifs, serving as templates for novel materials inspired by the poly-alanine domain within tropoelastin (Fig. 1b)[10]. We

[1]Nanoscience Center, Department of Physics, University of Jyväskylä, Jyväskylä, Finland. [2]VTT Technical Research Centre of Finland Ltd., Espoo, VTT, Finland. [3]These authors contributed equally: Zhuoran Geng, Timo Laakko, Ari Hokkanen. e-mail: Pezhman.mohammadi@vtt.fi

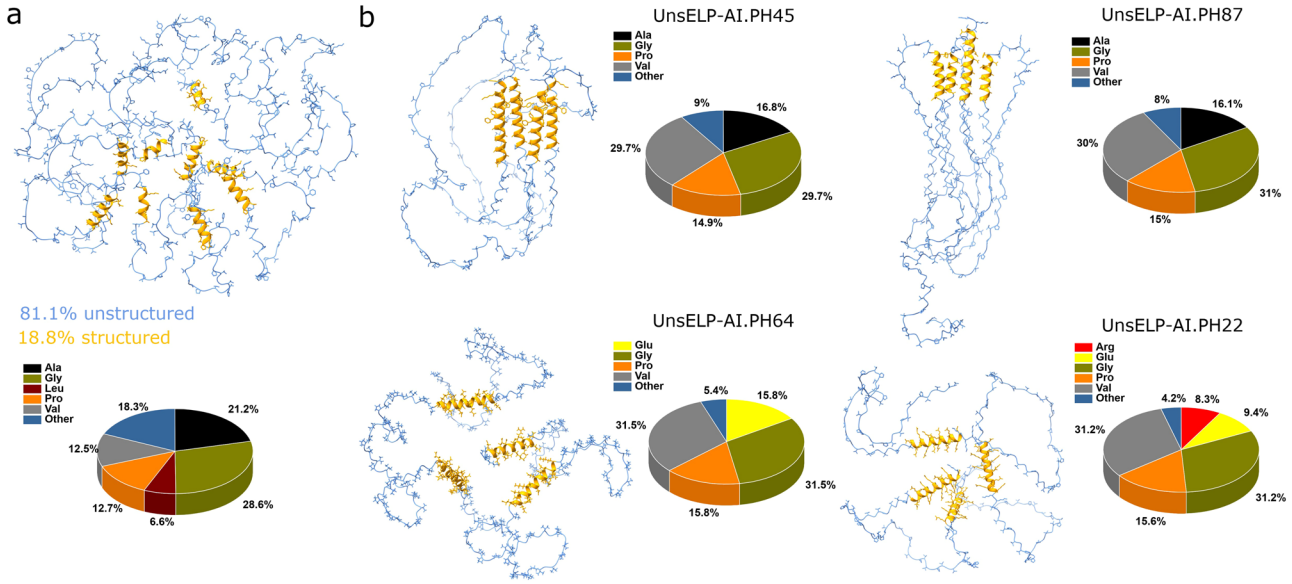

Fig. 1 | Machine learning assisted design of hybrid biomimetic-de novo ELP variants. a AlphaFold predicted the structure of human-origin tropoelastin (P15502_ELN-HUMAN). The unstructured regions are colored blue and the structured regions (α-helical) are orange. The pie chart demonstrates the most abundant amino acids found in tropoelastin. Amino acids with less than 5 % abundance are grouped into "Other". **b** Four of the best performing AIMS predicted hybrid biomimetic-de novo design ELP variants[10]. The "UnsELP" stands for the unstructured region of an elastin-like polypeptide (UnsELP), the "AI.PH$_n$" stands for AIMS predicted helices, and the "n" is the identification number of the helix.

showed these motifs would retain their structural integrity and functionality yet surpass their natural counterparts in terms of molecular stability, thereby accommodating various technical applications such as self-modulating compounds in smart windows for regulating solar radiation and programable thermoresponsive tissue injectable matrix with prolonged self-assembly or rapid disassembly[10]. For that, we combined multiscale computational modeling (MCM) and Convolutional Neural Network (CNN) deep neural network models. The de novo designs were incorporated into well-studied intrinsically disordered pentapeptide repeating motifs found in tropoelastin. Subsequently, the newly engineered protein variants were produced through recombinant methods. Various experimental assessments confirmed that all integrated de novo helices retained their predicted structural conformations. Moreover, the new variants demonstrated modifiable supramolecular self-assembly behavior and phase properties, a phenomenon examined both computationally and empirically.

In this study, we expanded the use of some of these previously discovered hybrid biomimetic-de novo ELP variants illustrated the effective translation of the predicted molecular designs in structural and functional materials and envisioned their use in high-added-value applications (Fig. 1b). To prove our concept, we selected four variants (named UnsELP-AI.PH45, UnsELP-AI.PH87, UnsELP-AI.PH64, and UnsELP-AI.PH22) and tested their potential use in multiscale drug delivery systems designed for controlled release, versatile wound dressings with multiple functions, and biobased photoresists that work exclusively in aqueous environments for large-area surface micropatterning or printing complex structural geometries with nano-and micrometer structural, as well as potential use for the development of flexible protein-based micro-robotics. We anticipate that the biosynthetic production of these protein materials will commence with the proposed approach, marking the inception of a fresh era in material design and engineering, and opening pathways to uncover novel structural proteins.

Results and discussion

AIMS predicted hybrid biomimetic-de novo design ELP variants

Tropoelastin, which acts as a precursor to elastin, shows strong parallels with other high-performance protein-based fibrous materials[9]. Structurally, it features a pattern of largely unorganized hydrophobic sequences (~80%), interspersed with organized hydrophilic segments (~20%). These hydrophobic sections are rich in short peptide sequences dominated by proline (Pro), glycine (Gly), and valine (Val), which induce flexibility and structural variation[9]. In contrast, the hydrophilic areas are primarily made up of alanine (Ala) and lysine (Lys), arranged in conserved stretches of 12–21 residues that form α-helices. Cross-linking within these helices contributes to the elasticity and recoil properties typical of elastin-containing tissues[9].

In our previous work, we introduced a predictive design framework utilizing AI-driven material science (AIMS) to craft sequences with de novo designed α-helical structures as guest motifs, taking inspiration from the poly-alanine regions in tropoelastin (Fig. 1b)[10]. This was achieved by integrating multiscale computational modeling (MCM) with Convolutional Neural Network (CNN) deep learning approaches. These motifs were shown to maintain their structural characteristics and outperform their natural analogs in stability, making them suitable for various applications such as self-regulating compounds in smart windows for solar radiation control and programmable thermoresponsive injectable matrices for tissue engineering[10]. The novel designs were incorporated into established intrinsically disordered pentapeptide repeats from tropoelastin. These engineered protein variants were then synthesized using recombinant techniques. Experimental validation confirmed that the newly designed helices preserved their intended structural forms. Additionally, the engineered variants displayed adaptable self-assembly and phase behaviors, confirmed through both computational and empirical studies[10].

In this work we selected four best-performing AIMS-designed hybrid biomimetic-de novo ELP variants[10]. These were named UnsELP-AI.PH45, UnsELP-AI.PH87, UnsELP-AI.PH64, and UnsELP-AI.PH22. The term "UnsELP" refers to the unstructured segment of an elastin-like polypeptide, while "AI.PHn" represents AIMS-predicted helices, with "n" denoting the specific helix identification number. The helices AI.PH22 (EEEEEREKEDEEEEEEEKKE), AI.PH45 (DAAAAAAAAAAYFHHAAAAKDAKK), AI.PH64 (EEERRREKERERREERRRKKK), and AI.PH87 (DAAAAAAAAAAKYHDAAAAAAKDAKK) exhibit diverse physicochemical properties. AI.PH22, with a molecular weight of 2.65 kDa and an isoelectric point (pI) of approximately 4.18, is highly hydrophilic due to its glutamic acid-rich sequence. AI.PH45 has a molecular weight of 2.74 kDa and a pI of 9.81, displaying moderate hydrophobicity because of its high

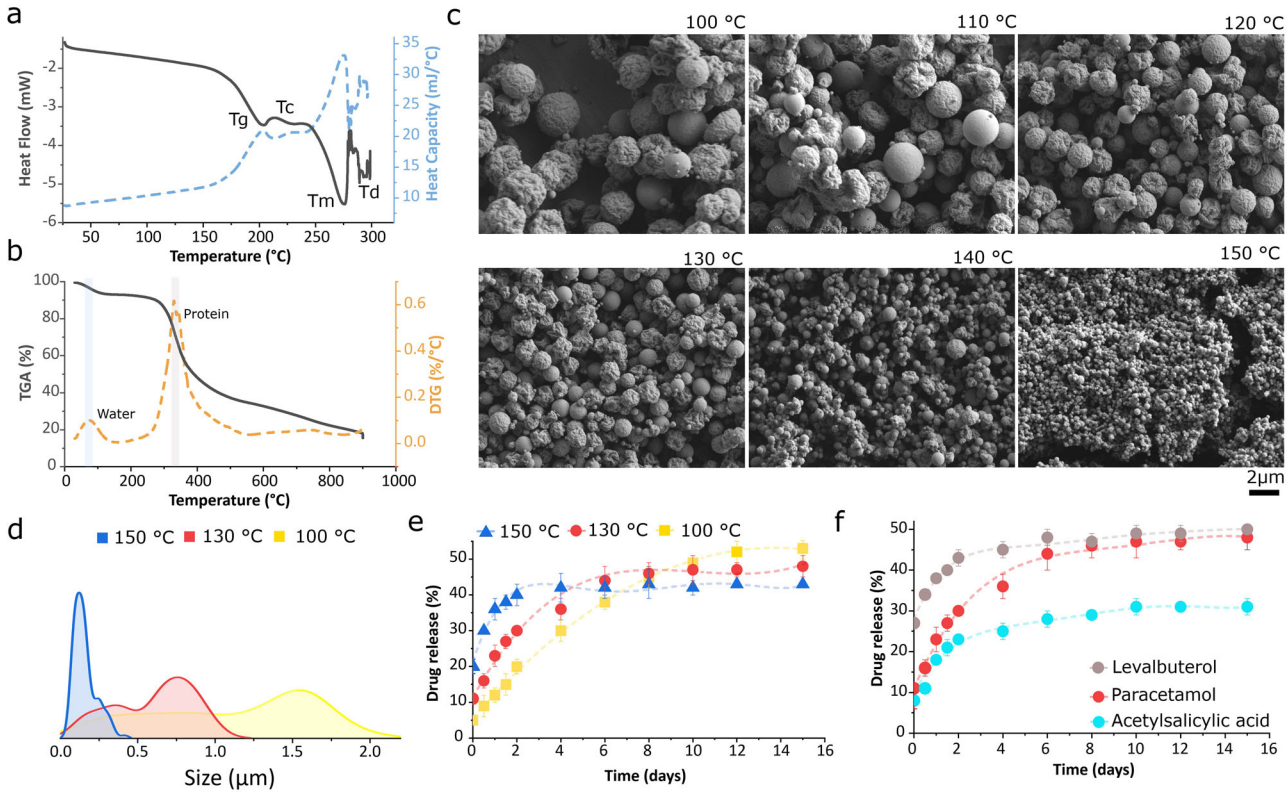

Fig. 2 | Nano-microspheres for drug encapsulation and controlled release. **a** Differential scanning calorimetry (DSC) of the UnsELP-AI.PH87 indicating its glass transition temperature (Tg), crystallization temperature (Tc), melting temperature (Tm), and degradation temperature (Td), **b** Thermo gravimetric analysis (TGA), as well as differential thermal analysis (DTG) corresponding to a. **c** SEM micrographs illustrating aerosol synthesized Nano and Micrometer size spherical particle made at six different temperatures below the critical glass transition of UnsELP-AI.PH87. **d** The particle size distribution for each formulation. **e** Mean and standard deviation of the paracetamol release profiles for the micro-nano particles fabricated at 100 °C, 130 °C, and 150 °C. **f** Mean and standard deviation of the release profile for levalbuterol and acetylsalicylic acid in addition to paracetamol with 130 °C fabrication parameter.

alanine and aromatic residue content. AI.PH64, weighing 3.10 kDa with a pI of 10.07, is characterized by its hydrophilic nature, attributed to a significant presence of charged residues like glutamic acid and lysine. AI.PH87, with a molecular weight of 2.84 kDa and a pI of 9.74, also shows moderate hydrophobicity, similar to AI.PH45, due to its composition mainly of alanine and lysine. These peptides feature a range of hydrophobic and hydrophilic characteristics, making them versatile for various applications involving elastin-like polypeptides.

To produce the full-length proteins, we utilized recombinant expression in *Escherichia coli* (E. coli) to genetically engineer these four de novo-designed ELP variants[10]. This involved incorporating fifteen repeats of the UnsELP sequence $(VPGVG)_{15}$, followed by a single AI.PHn unit. This combined segment, consisting of AI.PHn and $(VPGVG)_{15}$, was then repeated four times to construct the complete hybrid protein sequences.

Multiscale drug-encapsulating vehicles with controlled release

Nano-microspheres hold significant promise across wider scientific and commercial applications guiding advancements across a spectrum of disciplines and technology. These versatile particles exhibit potential in environmental conservation efforts by offering a sustainable alternative to microplastics, reducing the ecological footprint[1–4]. In cosmetics, they can serve as ideal carriers for active ingredients, enabling precise and controlled release, enhancing the efficacy of skin care products, or as fillers to offer a pathway to achieve smoother and more radiant skin[11]. In emulsion formulations for food, they can contribute to stability and uniform distribution of ingredients, improving product quality[12]. In the field of materials science, they can be used to enhance the properties of composites and coatings. Furthermore, nano-microspheres assume crucial functions in the domain of drug delivery, serving as vehicles for the precise and extended release of pharmaceutical compounds[13–19]. In this context, our investigation focused on drug encapsulation methods to achieve tunable pharmacokinetics and biodistribution profiles with a prolonging retention period suitable for applications such as inhalers (Fig. 2). Moreover, our comprehensive assessment of cytocompatibility for all four selected variants (UnsELP-AI.PH45, UnsELP-AI.PH87, UnsELP-AI.PH22, or UnsELP-AI.PH64), as previously detailed, provided further compelling reasons why this application stands as one of the most suitable avenues for exploration[10]. These assessments have validated their suitability for potential biomedical applications, as they promoted cell adhesion, growth, and proliferation with no apparent cytotoxicity.

We fabricated nano-micrometer-spherical particles by using UnsELP-AI.PH87 variant. Synthesis was carried out using a collision-type jet atomizer connected to a heated laminar flow reactor and a Berner-type low-pressure impact fractionator. To address the necessity for elevated temperatures during synthesis and gain a detailed understanding of UnsELP-AI.PH87's temperature responses under standard atmospheric conditions, we initially conducted a series of analyses including differential scanning calorimetry (DSC), thermal gravimetric analysis (TGA), and differential thermal analysis (DTG) (Figs. 2a, b). The results showed that UnsELP-AI.PH87 displayed a glass transition temperature (Tg) ranging from 175 to 200 °C, a crystallization temperature (Tc) in the range of 200–250 °C, a melting temperature (Tm) between 250–275 °C, and a degradation temperature (Td) exceeding 275 °C (Fig. 2a). The TGA and DTG profiles revealed two distinct weight loss events (Fig. 2b). The first, a minor peak at approximately 75 °C, likely attributed to the release of entrapped moisture, and the second, a more prominent peak at 320 °C, signifying substantial decomposition of UnsELP-AI.PH87.

Based on the insights gained, we proceeded with the synthesis at six distinct processing temperatures, all falling below the critical glass transition temperature of UnsELP-AI.PH87, spanning the range from 100 °C to 150 °C with the expectation of obtaining spherical morphologies of differing sizes. Anticipatedly, particle size exhibited an inverse correlation with flow reactor temperature, with higher temperatures resulting in smaller particles, and vice versa (Fig. 2c, d). High-resolution SEM images showed sizes ranging from ~20 nm to ~3 μm in diameter with mainly wrinkled surface morphology.

As the next step, we selected three ligands for drug release experiments, this includes acetylsalicylic acid, paracetamol, and levalbuterol (Fig. 2e, f). The selections were made due to adequate water solubility and being well-characterized in our previous work[20]. We then set to explore the effect of particle size on the release profile. For that, we incorporated paracetamol into the UnsELP-AI.PH87 formulation in one pot, facilitating its encapsulation within the spherical particles during the synthesis (Fig. 2e). The drug release profiles for particles synthesized at different temperatures (100 °C, 130 °C, and 150 °C) are depicted in the figure. Particles produced at 150 °C, which are the smallest in size, exhibit the fastest initial drug release, reaching approximately 40% within the first 2 days and eventually plateauing near 50% over 15 days. In comparison, particles synthesized at 130 °C show a moderate release rate, achieving around 30% release within the initial 2 days and reaching a plateau of approximately 48%. The largest particles, synthesized at 100 °C, display the slowest drug release, with about 20% released in the first 2 days and a maximum of just over 50% over the same period. These observations indicate a clear trend where higher synthesis temperatures, resulting in smaller particle sizes, correlate with faster drug release. It is important to note that while smaller particles indeed show faster initial release, the cumulative release over time reaches a plateau that may not exceed the total release of larger particles. Further examination revealed that depending on the ligands, the release profile varies likely due to their molecular size, hydrophobicity, and the strength of their interactions with the UnsELP-AI.PH87 (Fig. 2f).

The particle size plays a critical role in the drug release profile due to several factors. Smaller particles, synthesized at higher temperatures, have a higher surface area-to-volume ratio, which facilitates faster diffusion of the encapsulated drug. This increased surface area allows more drug molecules to be in contact with the release medium, enhancing the release rate. Additionally, the shorter diffusion path length within smaller particles means that the drug can travel more quickly from the interior to the exterior. Structural integrity and porosity of the particles are also significant factors. Smaller particles might have less structural integrity and higher porosity, which allows solvents to penetrate more easily, leading to quicker degradation or dissolution and consequently faster drug release. Conversely, larger particles, synthesized at lower temperatures, tend to have greater structural integrity and lower porosity, making them more stable and resistant to quick degradation. This results in a slower, more sustained release of the drug. These combined effects underscore the importance of controlling particle size through synthesis temperature to tailor drug release profiles effectively.

Multifunctional non-woven assemblies

Non-woven nano-microfibers, characterized by their exceptionally fine and interconnected structure, offer an array of alternative applications, harnessing their remarkable properties for diverse purposes[21,22]. In personal care and hygiene, they are increasingly employed in the fabrication of facial masks, providing superior breathability and filtration capabilities[23]. As the COVID-19 pandemic unfolded, their significance grew significantly, playing a pivotal role in containing the spread of the Coronavirus and saving lives[24]. Moreover, their adaptability for air and water filtration systems has revolutionized these sectors, enhancing efficiency in capturing contaminants[25–27]. In household appliances like vacuum cleaners, their inclusion as filters ensures cleaner air emissions. The textile industry benefits from these nanofibers, as they enable the creation of fabrics with tunable air permeability, enhancing comfort and functionality[28]. Furthermore, food packaging applications benefit from their versatility, extending the shelf life of products and minimizing microbial contamination[29–31]. The adaptability of nonwoven nanofibrils extends to the healthcare industry, where their unique properties contribute to improved patient care and device performance for example in wound coverage and medical devices, such as filters and sensors, to enhance their performance and durability[32–35].

In wound care applications, nanofibrous materials are utilized to fabricate advanced bandages and dressings that offer customizable breathability and conformability[36–40]. These materials exhibit a dual functionality, serving both as a physical barrier and a delivery system for therapeutic agents. The primary advantage lies in their ability to act as a barrier against external contaminants while simultaneously delivering antimicrobial compounds and growth factors directly to the wound site[41,42]. This dual role enhances wound healing efficiency by not only protecting the wound from infection but also actively promoting tissue regeneration and repair[43]. The nanofibrous structure allows for the controlled release of these therapeutic agents, providing sustained antimicrobial activity and supporting the healing process over time. Additionally, the high surface area-to-volume ratio of nanofibers facilitates the absorption and retention of exudates, keeping the wound environment moist and conducive to healing[36–40]. The integration of antimicrobial agents within these materials further reduces the risk of bacterial colonization and biofilm formation, a common complication in chronic wounds. By incorporating growth factors, these dressings can stimulate cellular activities such as proliferation and migration, accelerating the re-epithelialization and remodeling phases of wound healing.

Similarly, we also took the challenge of making similar structurally stable scaffolds from nonwoven fibers (Fig. 3). Using an electrospinning setup and blend of UnsELP-AI.PH45/polyethylene oxide as the spinning dope, we fabricated diverse nonwoven morphologies that exhibited very distinct release profiles, mechanical strength, and flexibility by alternating the solution as well as the spinning conditions (Fig. 3a). This ranged from Nano-filaments (NF), nano-ellipsoids on nano-filaments (NEF), micro-filaments (MF), micro-beads on micro-filaments (MBF), micro-ellipsoids on micro-filaments (MEF), and beads (B).

Formulation B was prepared by dissolving UnsELP-AI.PH45 in 1-butanol to create a 20% w/v spinning dope with a pH of 7.4. The electrospinning conditions included a spinning voltage of 20 kV, a needle gauge of 20, a spinning distance of 17.5 cm, and a flow rate of 1 ml/h. Similarly, the MBF formulation was generated using UnsELP-AI.PH45 dissolved in hexafluoroisopropanol (HFIP) to achieve a 20% w/v concentration with a spinning dope pH of 11. The electrospinning parameters were the same as for Formulation B. MEF was prepared using a blend of 0.7% w/v PEO in MilliQ water and protein-HFIP at a 50% w/v concentration, with a spinning dope pH of 7.4. The electrospinning conditions included a spinning voltage of 17 kV, a gauge of 18, a spinning distance of 10 cm, and a flow rate of 0.5 ml/h. NEF was created using a mixture of 0.7% w/v PEO-MQ and protein-HFIP at a 50% w/v concentration, with the same electrospinning parameters as MEF. For NF, the spinning dope consisted of 1% w/v PEO-MQ and protein-HFIP at a 20% w/v concentration. The electrospinning process involved a spinning voltage of 21 kV, a needle gauge of 20, a spinning distance of 15 cm, and a flow rate of 0.25 ml/h, with a spinning dope pH of 7.4. Lastly, the MF formulation was created using 1% w/v PEO-MQ and protein-HFIP at a 20% w/v concentration, with the same electrospinning parameters as Formulation B.

Using high-resolution SEM, we examined a range of fabricated micro- and nano-structures, each with distinct morphologies and surface characteristics (Fig. 3a). MF shows a dense network of interwoven filaments, forming a highly entangled fibrous mat that provides extensive surface area and mechanical support. MBF consists of spherical beads uniformly distributed on the filaments, enhancing the fibrous network with smooth and uniform surface characteristics, adding discrete functional points. NEF features elongated ellipsoid nanoparticles attached to thinner, entangled filaments, increasing surface area and functional capabilities while maintaining a smooth and consistent surface texture. MEF displays larger ellipsoid particles distributed across the filaments, creating a hybrid structure that combines macro and micro-scale features for potentially enhanced

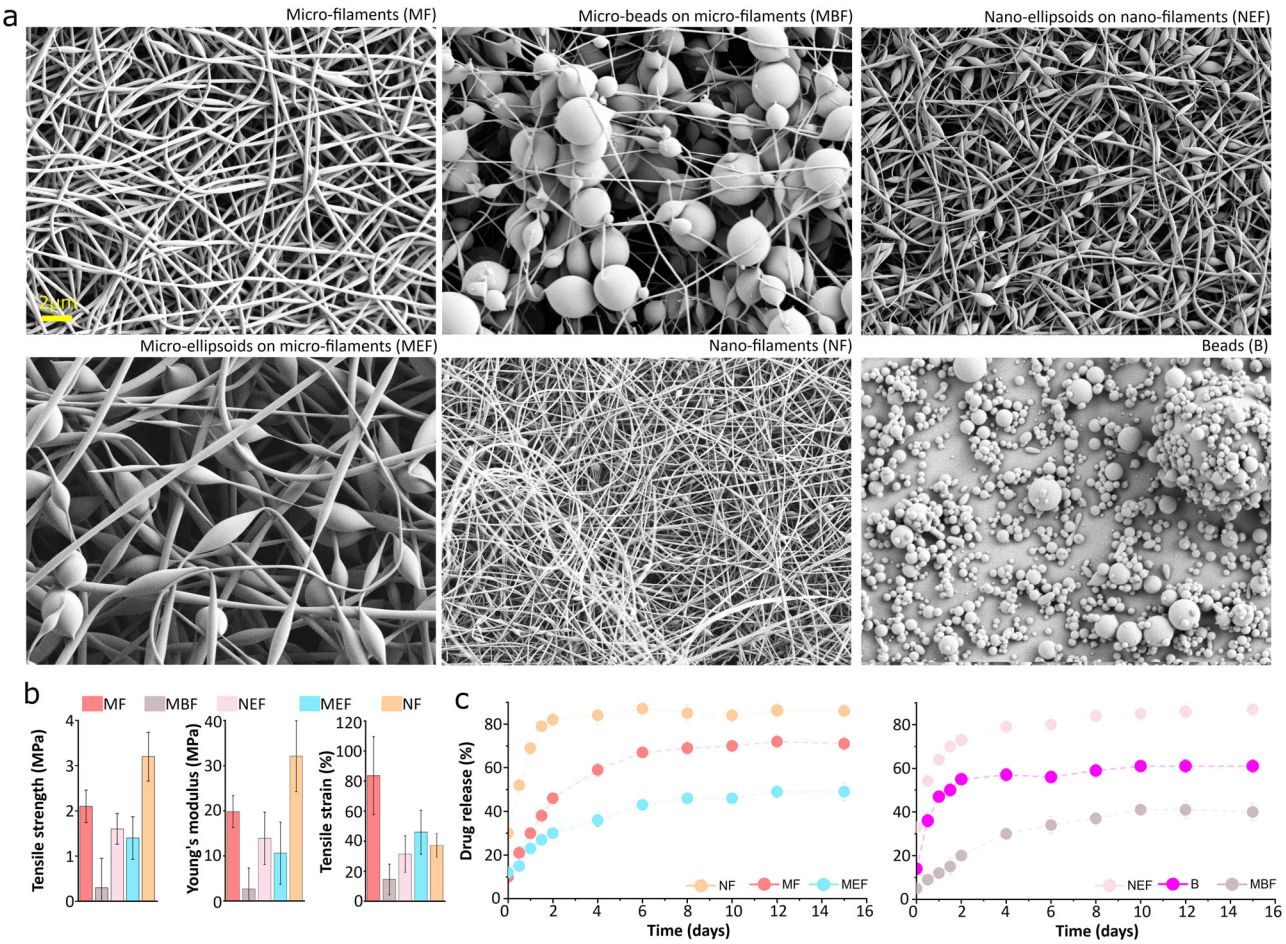

Fig. 3 | Various electrospun morphologies with maintained structural integrity for use in drug encapsulation with controlled release. a SEM micrographs of different electrospun morphologies of UnsELP-AI.PH45 including microfilaments (MF), micro-beads on micro-filaments (MBF), nano-ellipsoids on nano-filaments (NEF), micro-ellipsoids on micro-filaments (MEF), Nano-filaments (NF) and beads (B). **b** Mean and standard deviation for tensile strength, Young's modulus, and tensile strain of morphologies corresponding to (**a**). **c** The paracetamol release profiles from the morphologies corresponding to panel a.

mechanical properties, also characterized by uniform surfaces. NF presents a dense mesh of thin, intertwined filaments, forming a fine network with significant surface area and porosity, suitable for applications requiring high reactivity or surface interaction, and exhibiting smooth filament surfaces. B comprises densely packed spherical beads with smooth surfaces, forming a compact layer ideal for applications needing a homogeneous particle arrangement. Each structure leverages its unique morphology and surface smoothness, contributing to its potential application in various scientific and industrial fields.

To gain deeper insights into the mechanical characteristics of all examined formulations, tensile measurements were conducted as depicted in Fig. 3b. We were unable to perform mechanical property assessments on formulation B due to its powdered form. Among the tested formulations, NF stands out with the highest tensile strength of 3.2 MPa, a Young's modulus of 32.1 MPa, and a tensile strain of 87.65%. Following closely is the MF formulation, which demonstrates the second-highest tensile strength at 2.1 MPa and a tensile strain of 1.78%. However, its Young's modulus, while still relatively high at 19.8 MPa, is lower than that of NF. Moving on the NEF formulation exhibits moderate tensile strength at 1.6 MPa and a Young's modulus of 13.9 MPa. However, its tensile strain remained at 41.14%, lower than MF. MEF, on the other hand, presents a tensile strength of 1.4 MPa and a Young's modulus of 10.6 MPa, both of which were lower than NEF. Notably, its tensile strain, standing at 34.84%, surpasses that of NEF. In contrast, the MBF formulation displays the lowest tensile strength, a mere 0.3 MPa, along with a Young's modulus of 2.65 MPa and a tensile strain of 14.6%. In a general sense, materials with higher tensile strengths tend to exhibit higher Young's moduli, as these properties are closely linked to a material's stiffness. However, there is no absolute correlation between the two attributes. For instance, while MF boasts a higher tensile strength than NEF, Young's modulus was lower, suggesting that MF may possess greater brittleness compared to NEF. Finally, the recorded standard deviations for all reported mechanical properties were generally high, indicating considerable variability within each material group.

We then looked into drug release profiles for all the formulations (Fig. 3c). We tested the drug release profiles over 16 days for various fabricated structures. Each structure demonstrates distinct drug release behaviors, potentially influenced by their unique morphologies. NF and MF, with their highly entangled fibrous networks, show rapid initial drug release, reaching approximately 80% and 70%, respectively. This rapid release is likely due to their extensive surface area and porous nature, which facilitate quicker drug diffusion. MEF, characterized by larger ellipsoids on microfilaments, shows a moderate release profile, achieving around 40%, possibly due to the combination of micro-scale features that could offer a balance between surface area and structural density, moderating the diffusion process. On the other hand, MBF, which incorporates micro-beads on filaments, exhibits release rates of about 30%, respectively. Their more complex morphology, combining micron-sized beads or ellipsoids with filaments could potentially create additional diffusion pathways and barriers, potentially slowing down the release process in the case of MBF. In contrast, the presence of nano-sized ellipsoids as in NEF produces a release profile similar with negligible differences to NF, achieving approximately 80% maximum release and maintaining a plateau for the remainder of the

measurement period. However, the initial release proved to be slower, reaching around 70-75% within the first two days, conversely, whereas this was 80% in the case of NF. B, comprising densely packed spherical beads, displays the slowest release profile, achieving around 50%. The compact and uniform surface of the beads likely limits the available surface area for drug diffusion, resulting in a slower release rate. We found this to be in good agreement with the drug release profile for the Nano-microspheres described in the previous section ranging from 40 to 50% (Fig. 2)

These differences between the various fabricated structures using electrospinning can be attributed to several factors. The primary influence is the morphological characteristics of each structure, such as surface area, porosity, and the presence of diffusion pathways. Structures with higher surface area-to-volume ratios, like NF and MF, allow for faster drug release due to increased exposure of the drug to the release medium. Additionally, particle size and distribution may play roles; in smaller or more interconnected particles. The high-resolution SEM images reveal that in the NEF structure, densely packed nano-filaments intertwined with nano-ellipsoids create a highly intricate and convoluted network. This architectural complexity, despite the high tortuosity, results in a high release profile due to the small size and large surface area of the nano-ellipsoids, which facilitate faster diffusion and higher overall drug release.

In contrast, MBF tends to slow the release potentially due to more complex diffusion routes. The high-resolution SEM images reveal that in the MBF structure, micro-beads attached to micro-filaments form an interconnected matrix with numerous junctions, confined passages, and overlapping layers with extended diffusion pathways, as drug molecules encounter numerous points of resistance and interaction throughout the network. The structural heterogeneity within these matrices significantly impedes molecular mobility. The larger size and lower surface area-to-volume ratio of the micro-beads further contribute to the reduced effective diffusivity and slower drug release. A crucial factor in these observations is the ratio of spheres to filaments. In the MBF structure, the ratio of micro-beads to micro-filaments is higher, resulting in fewer active diffusion sites and longer diffusion pathways, which slows down the release rate. All these complexities increase the tortuosity of the diffusion pathways, thereby reducing the effective diffusivity of the drug molecules through the system.

The density and compaction of the structures may also affect release rates, with more densely packed beads (as in B) providing fewer pathways for the drug to diffuse, thus slowing the release process. Furthermore, the swelling behavior of the material upon contact with the release medium might enhance drug release by increasing surface area or opening additional pathways in our case. Entrapment efficiency influences how much drug is available for release, with higher efficiency might prolong the release. Finally, the matrix degradation rate plays a crucial role, as faster-degrading matrices may lead to quicker drug release while slower-degrading ones provide more sustained release.

These are only some of the major mechanisms that could be responsible for the observed differences in drug release. To fully understand these phenomena, future studies are needed to investigate also additional factors such as the chemical interactions between the drug and the polymer matrix, the influence of environmental conditions on drug stability, and the impact of long-term degradation on release profiles. Advanced analytical techniques and in-depth kinetic modeling will be crucial to comprehensively elucidate the intricate processes governing drug release. This broader exploration will enhance our ability to design optimized drug delivery systems tailored to specific therapeutic needs and material properties in the future.

To summarize, the choice of structural morphology for a particular drug delivery application will depend on the desired release profile. For example, a rapid-release material may be desired for a drug that is needed to take effect quickly. An intermediate-release material may be desired for a drug that is needed to maintain a therapeutic level in the body for a period of several days. A sustained-release material may be desired for a drug that is needed to maintain a therapeutic level in the body for a period of several weeks or months. Overall, the six materials exhibit a wide range of structural morphology, mechanical, and release profiles. Therefore the choice of material for a particular application could be fine-tuned for specific requirements of that application.

All-aqueous-based biobased photoresists

Photoresists are pivotal materials in photolithography, a process fundamental to fabricating intricate patterns on substrates for semiconductor devices, microelectromechanical systems (MEMS), and advanced circuit boards just to name a few[44]. These materials are formulated with light-sensitive compounds that undergo chemical changes upon exposure to light, allowing for the precise transfer of patterns onto substrates. Traditionally, photolithography employs a mask to selectively expose areas of a photoresist-coated substrate to light, which is followed by development to reveal the pattern for subsequent etching or deposition. Beyond traditional mask-based lithography, advanced techniques such as two-photon lithography are gaining prominence. Two-photon lithography enables high-resolution 3D printing by focusing femtosecond laser pulses to induce polymerization within a photoresist, allowing for the creation of complex 2D and 3D microstructures without the need for a mask. This method is particularly advantageous for fabricating micro- and nanoscale devices with intricate geometries and is used in fields such as microfluidics, biomedical engineering, and photonics[44].

The urgent transition to all-aqueous-based biobased photoresists is critical for reducing the environmental footprint of photolithography associated with conventional petroleum-based photoresists, enhancing operator safety, and fostering innovation in sustainable and biomedical technologies[45–47]. As the name suggest, all-aqueous-based biobased photoresists utilize water and renewable polymers, offering a sustainable and safer alternative. Their biocompatibility makes them particularly valuable for biomedical applications, including cell culture platforms, tissue engineering scaffolds, and microfluidic devices. By facilitating the fabrication of biocompatible structures, they open new avenues for creating complex tissue models and bio-integrated devices, essential for advancing medical research and therapies[45–47].

In light of this, we explore the use of UnsELP-AI.PH$_n$ as the next-generation biocompatible and biodegradable photoresist. Given the high molecular stability of the UnsELP-AI.PH$_n$ and resistance to increase in the solution temperature, we hypothesized the UnsELP-AI.PH$_n$ withstands exposure to the high-energy light source without undergoing molecular degradations. This exploration involves the use of water as a solvent, eliminating the necessity for any harmful or noxious chemicals. Initially, we decided to evaluate this hypothesis through the application of a conventional 2D photolithography technique, primarily for wide-area surface patterning, as visually depicted in Fig. 4[48–50]. To achieve this, we employed various photomasks, allowing us to generate an array of diverse microstructures using UnsELP-AI.PH64. This was accomplished by exposing the spin-coated substrates to a high-intensity laser beam (532 nm) and Rose Bengal as the photoinitiator, with power levels ranging between 900 and 1000 mW. While our primary objective in this phase wasn't to perform cell culture or tissue engineering experiments on these patterned surfaces, our prior research had already highlighted the potential use of UnsELP-AI.PHn in cell adhesion and viability[10]. Therefore, it's crucial to emphasize that the outcomes of these patterning experiments could lay the groundwork for what was previously identified as a promising avenue of research in the fields of cell culture and tissue engineering with innovative possibilities that lie ahead in these areas[48–50].

To better test the capability of our engineered photoresist for printing, we then used the state-of-the-art two-photon polymerization setup for the microfabrication of various shapes and morphologies (Fig. 5)[51,52]. For that we employed the use of UnsELP-AI.PH22. The result revealed the suitability of the ink for printing stable 3D structures with substantial complexities such as photonic crystals and woodpile structures with feature resolution of ~100 nm (Fig. 5a). All the printed geometries maintained their structural integrity both in solution and after drying capable of resisting vigorous washing treatments. A less obvious aspect worth highlighting is a distinctive advantage in terms of its low viscosity and free-flowing consistency[52,53]. This property is primarily attributed to the relatively low protein concentration (50 mg/ml) within our

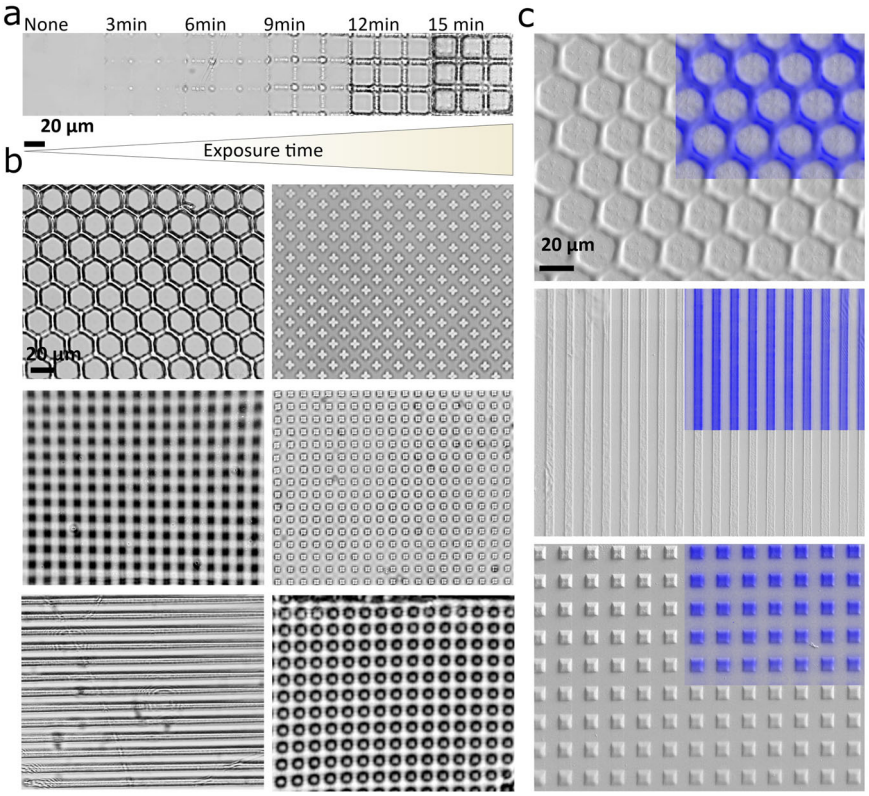

Fig. 4 | Next-generation biocompatible and biodegradable photoresist. a Large area surface micropatterning using conventional 2-dimensional mask-based photolithography approach using UnsELP-AI.PH64 as the photoresist. The panel shows bright field microscopy images at various exposure times. **b** Surfaces that are patterned with various shapes. **c** SEM micrographs of three surface patterns. For better visibility fluorescent images (falsely colored blue) are overlaid on top of gray-scaled micrographs.

formulation. It stands in stark contrast to the commercially available products, which often exhibit high viscosity and denser consistency, attributes primarily stemming from its comparatively low protein concentration. This contrast is particularly noteworthy in applications, including those that involve the intricate printing of geometries within confined spaces, such as microfluidic systems[45,54]. In such settings, where precision and accuracy are of paramount importance, the advantages of our low-viscosity ink become evident by facilitating even infiltration of micron-size channels and other confined intricate geometries. Moreover, this benefit extends beyond the printing process. In microfluidic systems, removing undeveloped monomers or residues left behind by the printing ink can be a considerable challenge, often requiring extensive washing steps or harsh reagents[45,48,51–54]. Our low-viscosity ink's advantage eases the removal process and minimizes the potential for clogs commonly associated with high-consistency inks.

We further set to explore the microfabrication of soft protein-based micro-robots, affectionately termed "protobots" in our study, with the envisioned potential applications in targeted delivery and diagnostics (Fig. 5b). It's important to note that our focus at this stage was primarily on the conceptualization and early development of these micro-robots, and while certain aspects were untested, we see significant promise in their future possibilities. The miniature scale of these protobots, coupled with the non-cytotoxic and biodegradable building materials, lays a promising foundation for their translation into clinical applications. This transition brings the advantage of tunable interactions with tissues, enhanced device integration, and the potential for minimal immune responses. Our initial microfabrication efforts shaped the protobots into the form of a double spiral drill bit (DSDB), which, in theory, holds the capability for rapid-forward velocity propulsion when acted upon by torque generated by superparamagnetic nanoparticles under the influence of rotating magnetic fields, as previously described[55]. Although we did not perform these specific propulsion experiments, they serve as a proof of concept, illuminating the potential for steering and actuation of DSDB-protobots through external stimuli, such as magnetic fields, along predefined trajectories. In our vision, the protobots described in this work, comprised of more than 99% protein, are designed for eventual proteolytic enzymatic degradation once their intended tasks are accomplished. While we have yet to conduct enzymatic degradation tests, we foresee that this property could play a pivotal role in mitigating any potential long-term accumulation of these micro-robots within the body, thereby avoiding undesirable chronic inflammation. The concept is that the body's natural waste management system could, in the future, decompose these protobots into their smallest constituent building blocks. In essence, our current work represents a proof of concept, demonstrating the exciting potential applications of protobots in the context of targeted delivery and diagnostics, with our focus shifting towards further validation and development in subsequent stages.

In conclusion, the reproducibility of the printed structures has been thoroughly validated using both 2-photon lithography and conventional mask-based photolithography. The 2-photon lithography demonstrated consistent replication of intricate micro-scale shapes, confirming the technique's ability to produce detailed 3D structures reliably across multiple iterations. Conversely, the mask-based photolithography allowed for large-area surface patterning, where systematic variations in exposure time resulted in predictable and reproducible pattern formations. The robustness of these methods was corroborated through repeated experiments conducted under controlled conditions, with reproducibility verified using advanced imaging techniques such as SEM, light, and fluorescence microscopy. These imaging methods consistently confirmed accurate structural dimensions and pattern fidelity, underscoring the reliability of both fabrication techniques in generating precise and reproducible micro-scale structures.

Conclusion

Inspired by high-performance protein-based biomaterials such as silk and elastin, we've honed our attention on Elastin-like polypeptides (ELPs). ELPs, mirroring tropoelastin's characteristics, offer exceptional mechanical properties, including resilience, elasticity, and toughness, making them invaluable for durable and long-lasting materials. Their biocompatibility and biodegradability are crucial in medical and biological contexts, and their renewable sourcing through biosynthesis in microbial systems adds an extra layer of sustainability. Expanding on our prior work, we've demonstrated the potential use of four best-performing hybrid biomimetic-de novo ELP

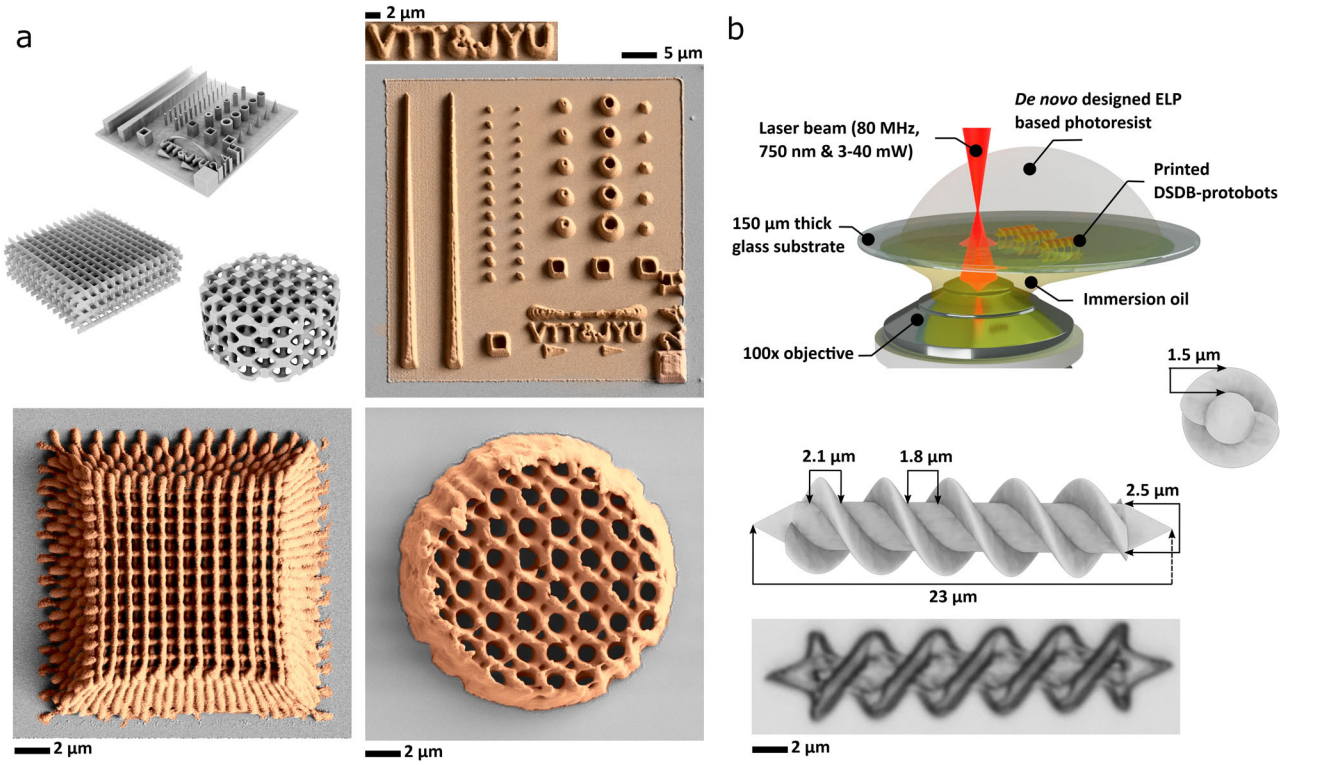

Fig. 5 | 3-dimensional printing through the use of a 2-photon lithography system. **a** 3D printing complex structural geometries with nano-and micrometer structural features by using the UnsELP-AI.PH22 as the photoresist. Shapes include pillars, cones, cubes, square-based pyramids but also photonic crystals and woodpiles. Grayscale images were falsely colored for better visibility. **b** Schematic representation of printing setup for manufacturing soft protein-based micro-robots (named in our work as "protobots"). The panel also demonstrates the shape and dimension of the protobots (side and top view) as well as a light microscopy image of one of the printed protobots.

variants assisted by AI-empowered material design workflow. They tested in multiscale drug delivery systems, versatile wound dressings, biobased photoresists for surface micropatterning, and flexible protein-based microrobotics. As we move forward, we foresee the biosynthetic production of these protein materials marking a new era in material design and engineering. This innovation opens pathways to discover novel structural proteins, reinforcing our commitment to sustainable, high-performance materials with a wide array of applications and presenting promising solutions to address the pressing environmental challenges of our time.

Methods

AIMS deep neural network architecture and molecular dynamic simulation

The AIMS protocol for generating de novo design sequences with α-helical conformations assisted by the AIMS deep learning model is comprehensively described in our previous work[10]. Briefly, the protocol comprises three main components: AIMS-GATHER, AIMS-GENERATE, and AIMS-PROT. AIMS-GATHER conducts data mining to identify homologous templates based on expert-provided sequences or structural information. If it can't find homologs, it uses the DSSP algorithm to estimate structural conformation. AIMS-GATHER supplies training data for AIMS-GENERATE and AIMS-PROT, both deep neural network models. In the next step, AIMS-GENERATE is trained with a dataset of 95,000 proteins, learning properties like hydrophobicity, hydrophilicity, and more from amino acid content. It generates new sequences based on input secondary structure and property values, allowing for customization within limits. AIMS-PROT predicts dihedral angles and secondary structure for the generated sequences. Molecular dynamics simulation assesses structural stability. If accuracy falls below a threshold, sequences are excluded. The remaining sequences undergo MD simulation and similarity checks, ensuring only novel, stable sequences are considered.

Molecular cloning, protein production, and purification process

All sequences presented in this work optimized for efficient expression in Escherichia coli (E. coli). The constructs were made by the fusion between fifteen repetitions of the widely used unstructured ELP sequence (VPGVG) 15, and one of the four helices predicted by AIMS-PROT. This fusion was further repeated four times for each individual sequence, ultimately yielding full-length protein sequences named UnsELP-AI.PHn. The "n" in the nomenclature represents the identification number assigned to each predicted helix. To enable effective purification, all synthetic coding fragments were cloned in-frame with a C-terminal 6×His-tag. The cloning itself was executed through seamless golden gate assembly, meticulously performed in the pET-28a (+) (kanR) protein expression vector provided by Novagen. The cloning process involved the use of the 10-beta competent E. coli strain, specifically designed for cloning purposes. In our study, four distinct expression strains were utilized for protein production, including BL21 T7 express™ (New England Biolabs), BL21 Star™ (ThermoFisher Scientific), and ClearColi® BL21 (DE3) (Lucigen). Single colonies were meticulously picked from freshly prepared LB plates that had been cultivated overnight. The colonies were then inoculated into 5 mL of culture media, supplemented with kanamycin to support the growth of the engineered sequences. The 5 mL starting cultures were further incubated for 6–7 h, set at 37 °C and agitated at 250 rpm. Once the culture reached its optimal state, it was inoculated into 500 mL of fresh LB media, placed in a 2 L Erlenmeyer flask. The culture was then grown at 37 °C and agitated at 250 rpm for approximately 2–3 h, until the cells reached a mid-log phase, marked by an OD at 600 nm of approximately 0.4. At this stage, the expression process was chemically induced by the addition of 0.1 mM isopropyl β-D-1-thiogalactopyranoside (IPTG) from Sigma-Aldrich, and the temperature was reduced to 18 °C. The induced culture was allowed to grow for a period of 15–20 h, post-induction. Subsequently, the cells were harvested through centrifugation at 16,000 × *g* for 15 min, maintained at 4 °C. After this

process, the cells were either frozen and stored at −80 °C or kept at 4 °C, awaiting further downstream purification steps. To ensure the production of highly pure proteins, it was imperative to follow a robust purification process. The initial step in this purification process involved resuspending the cell pellets obtained from a 500 mL culture using 5 mL of Lysis Buffer. This buffer comprised essential components, including 20 mM 4-(2-hydroxyethyl)−1-piperazine ethane sulfonic acid (HEPES) (Sigma-Aldrich), pH 7.5, 200 mM NaCl (Sigma-Aldrich), 20 mM Imidazole (Sigma-Aldrich), 5 mM MgCl2 (Sigma-Aldrich), 0.5 mg/ml lysozyme (Sigma-Aldrich), 0.01 mg/ml DNase I (Sigma-Aldrich), and 1× SIGMA FAST protease inhibitor cocktail (EDTA). Following this, the cells were incubated with the lysis buffer for a duration of 45 min at 4 °C, with gentle rotation to facilitate even distribution of the lysis buffer. After this incubation period, sonication was performed using a Qsonica 500 instrument to physically disrupt the cells. The sonication process involved an amplitude input set at 20–30% and ran for 3 min, with 2-s intervals (ON-OFF cycle), while maintaining the cells at a low temperature by placing them on ice. Following sonication, the cell debris was isolated through centrifugation at 16,000 × *g* for 60 min at 4 °C and subsequently discarded. The soluble fractions were filtered once using 0.20 µm filters and were then prepared for purification through HisTrap FF immobilized metal affinity chromatography (IMAC). This chromatography was conducted using an ÄKTA-Pure fast protein liquid chromatography system, all operating at a controlled temperature of 4 °C. During the chromatographic process, the binding buffer consisted of 20 mM imidazole, 200 mM NaCl, and was adjusted to a pH of 7.4. The elution buffer, on the other hand, was formulated with 200 mM imidazole and 500 mM NaCl, also maintaining a pH of 7.4. The proteins of interest were subsequently eluted from the column through a gradient elution technique, skillfully controlled by a method crafted in UNICORN 7 software. This involved a gradual increase in the concentration of imidazole, ensuring the detachment of all bound proteins from the column. To further enhance the quality of the purified proteins, buffer exchange was carried out. This was achieved using Econo-Pac10 DG desalting prepacked gravity-flow columns from Bio-Rad, against 50 mM Tris-HCl, maintained at a pH of 7.4. The purified protein solutions, now of exceptional purity and quality, underwent three additional washing steps to ensure the highest level of purity. The final step in this process included concentration, achieved using 20 ml sterile Vivaspin 10 kDa protein concentrator spin columns. The protein concentration was determined by measuring the absorbance at 280 nm using a DS-11 FX Spectrophotometer. Furthermore, the size of the purified proteins was analyzed via sodium dodecyl sulfate-polyacrylamide gel electrophoresis (SDS-PAGE). This analysis was performed by running the samples through 4–20% gradient gels from Bio-Rad. Staining of the SDS-PAGE gels was conducted using Coomassie Brilliant Blue stain, with imaging facilitated by the Bio-Rad ChemiDocTM XRS Imaging System. It is important to note that, unless otherwise specified, all samples were diligently stored at −80 °C until they were ready for further analysis.

Scanning electron microscopy (SEM)

SEM imaging was performed using a Zeiss FE-SEM field emission microscope with variable pressure, operating between 1 to 2 kV. Before the imaging, all specimens were sputtered with a 2–3 nm platinum layer. ImageJ Fiji (version 1.47d) software was used for the visualization and analysis of the micrographs[56].

Differential scanning calorimetry (DSC)

About five milligrams of lyophilized samples were measured using an analytical scale into platinum alloy pans (TA Instruments, New Castle, DE, USA) and hermetically sealed and analyzed using a DSC instrument 250 (TA Instruments, New Castle, DE, USA). Pans with samples were equilibrated at 150.00 °C, isothermal for 1 min, then equilibrated at 25 °C heated followed by ramping up to 300 °C at 10 °C/min with the final step of equilibration at 40.00 °C. Nitrogen was purged in the DSC cell at 50 mL/min. Three replicates were analyzed per sample. The heating curves were analyzed with Universal Analysis Software (Version 3.9 A, TA Instruments).

Thermo gravimetric analysis (TGA) & differential thermal analysis (DTA)

The thermal degradation behavior of the cured samples was tested by using TA Q500 (TA Instruments, New Castle, DE, USA). About 5 mg of lyophilized samples sample weighted in a platinum alloy cup. The changes in the weight were recorded in a nitrogen-rich environment scanning from ambient temperature to 900 °C at a heating rate of 10 °C/min.

Aerosol micro- and nanoparticle synthesis

Collision-type jet atomizer with nitrogen gas feeding was used to synthesize the spherical particles with sizes ranging from ~20 nm to ~3 µm[57]. Synthesis was carried out by using 2% w/v proteins solution in 50 mM phosphate buffer (pH 7.4). The droplets were suspended at a nitrogen gas flow with a rate of 3 L/min connected to a heated (at 120 °C) laminar flow reactor. Droplets were dried into solid spherical particles during flow, which were subsequently cooled at the reactor downstream with 30 L/min air flow and fractionated simultaneously with a Berner-type low-pressure impactor consisting of 10 stages with nominal cutoff diameters ranging from 30 nm to 8 µm. For drug encapsulation, 5 mg of paracetamol was added to 1 ml of protein solution and allowed to dissolve completely overnight. For drug release studies 300 mg of the spherical particles were gently compressed in a tablet form. This was done to normalize the substantially large variation for the size of particles and minimize measurement error. Their release profile was quantified by equilibration in phosphate buffer - pH 7.0 for 15 days and reading the amounts of the drugs in the supernatant by measuring absorbances at 312.

Electrospinning

Various formulations were used to fabricate six diverse morphologies seen in Fig. 3. Unless otherwise stated either pure protein or a mixture of protein-polyethylene oxide (PEO) was used at different pH. Desired protein concentrations were obtained by dissolving lyophilized specimens in hexafluoroisopropanol (HFIP) or 1-butanol, whereas PEO was dissolved in Milli-Q water. The solutions were pumped through a 1 ml syringe connected to a needle (either 18 or 20 gauge) with a blunt end to an automated Fusion 4000 micro-syringe pump (Chemyx). The needle tip and the aluminum foil collector ground were both connected to a high-voltage source between 17 to 21 kV. The high voltage was applied to the needle tip and the collector ground while pumping the solution at various rates (0.2–1 ml/h) and a distance between the needle tip and the collector ground (cm).

For produced beads (B) following parameters were used: spinning dope protein 20 % w/v dissolved in 1-butanol, pH of the spinning dope 7.4, spinning voltage 20 kV, needle gauge 20, spinning distance 17.5 cm, spinning flow 1 ml/h. Micro-beads on micro-filaments (MBF): protein-HFIP 20% w/v, pH 11, 20 kV, gauge 20, 10 cm, 1 ml/h. Micro-ellipsoids on micro-filaments (MEF): 0.7% w/v PEO-MQ/protein-HFIP 50 w/v %, pH 7.4, 17 kV, gauge 18, 10 cm, 0.5 ml/h. Nano-ellipsoids on nano-filaments (NEF): 0.7% w/v PEO-MQ / protein-HFIP 50% w/v, 20 kV, needle gauge 18, 10 cm, 0.5 ml/h. Nanofilaments (NF): 1% w/v PEO-MQ / protein-HFIP w/v 20% 21 kV, needle gauge 20, 15 cm, 0.25 ml/h, needle gauge 20, pH 7.4. Microfilaments (MF): 1% w/v PEO- MQ/protein-HFIP w/v 20%, 20 kV, needle gauge 20, 10 cm, 1 ml/h, pH 7.4.

For drug encapsulation, 5 mg of either paracetamol, acetylsalicylic acid, or levalbuterol were added to 1 ml of spinning dope and allowed to dissolve completely overnight. Release profiles were quantified by equilibrating squired-shaped pieces (1 × 1 cm) in phosphate buffer - pH 7.0 for 15 days and reading the amounts of the drugs in the supernatant by measuring absorbances at 312, 330, and 220 nm respectively.

Laser lithography and surface micro-patterning

The optical setup equipped with 532 nm green DPSS with TTL Modulation High Power Pumped Laser (CivilLaser) with an output of 1000 mW equipped with an adjustable power supply and beam diameter of about 3 mm was used. The beam was expanded and collimated to approximately x10 using a beam expander in a form of Galileo telescope using a LC1054-A

N-BK7 Plano-Concave lens Ø1/2", f = −25.0 mm (AR coating: 350–700 nm), and AC254-250-A Achromatic Doublet lens, f = 250 mm, Ø1" (AR coating: 400–700 nm). All the lenses as well as the lens tubes, and internal and external threads were ordered from Thorlabs (USA). The desired micropatterns for the lithography were designed and fabricated by jd-photodata (United Kingdom) on a 4" Chrome Photomask (negative - right reading chrome down) with quartz as the base materials (90 mm^2 − 2.3 mm). The printing setup was built in an inverted format to carry out contact printing. Moving from the bottom to the top, the laser was placed upside down followed by the beam expander, beam aligner, photomask, and glass slide (22 mm^2, 0.13 mm thickness) on the top. The entire path length of the platform was 250 mm, whereas the distance of the laser source to the exposed area on the sample was between 220 and 230 mm unless otherwise stated. To print the micropatterns, 3ul Rose Bengal (100 mg/ml) as the photo cross-linker was intermixed with 27 µL of the desired protein sample (300 mg/ml). The mixture was vortexed before spreading it on the surface of the glass slide in direct contact with the photomask and exposed to a laser for 15 min at 900–1000 mW. Micropatterns were developed by immersing the glass slide under Milli-Q water, followed by sequential washing steps using 30%, 40%, 50%, 60%, and 70% v/v ethanol. Samples were then completely dried under nitrogen flow and stored in a desiccator until use.

3D lithography

The general setup of the printing of 3D microstructures is depicted in Fig. 5 with variations of structure models and exposure parameters. The 3D printing was done by using a direct laser writing system (Photonic Professional by Nanoscribe GmbH) with pulse rate of 80 MHz and a wavelength of 780 nm. A photosensitive aqueous mixture of the desired protein, Rose Bengal (Sigma-Aldrich), and ultrapure water was polymerized in the two-photon-absorption (TPA) process based on the designed 3D model of the microstructures. This solution was prepared by mixing 50 mg/ml and 20% wt. Rose Bengal both using water as the solvent. In each printing session, 75 µL protein mixture was dripped onto a 150 µm thick glass substrate (30 mm, No. 1, VWR), and an oil immersion objective (100x, NA = 1.4, Zeiss) was snapped from the backside of the substrate. The microstructures CAD designs were sliced into layers with 400 nm spacing in the direction normal to the substrate in the printing program, and these layers were then printed by the laser using a bottom-up approach beginning from the substrate-solution interface. The woodpile structures were printed with scan speed varying from 40 to 60 um/s, and laser power varying from 3 to 35 mW. The Logo and IWP structures were printed with a fixed scan speed of 40 um/s and laser power of 25 mW. After the printing, the samples were immediately developed in ultrapure water and then stored underwater until further use. It should be noted that the minimal development time we have used in the experiment is 30 min.

Data availability

All data needed to evaluate the conclusions in the paper are present in the paper. Any other data that support the findings of this study are available from the corresponding author upon reasonable request.

Received: 18 May 2024; Accepted: 2 August 2024;
Published online: 14 August 2024

References

1. Rillig, M. C., Kim, S. W. & Zhu, Y. G. The soil plastisphere. *Nat. Rev. Microbiol.* **22**, 64–74 (2024).
2. Rochman, C. M. & Hoellein, T. The global odyssey of plastic pollution. *Science* **368**, 1184–1185 (2020).
3. Stubbins, A., Law, K. L., Muñoz, S. E., Bianchi, T. S. & Zhu, L. Plastics in the Earth system. *Science* **373**, 51–55 (2021).
4. MacLeod, M., Arp, H. P. H., Tekman, M. B. & Jahnke, A. The global threat from plastic pollution. *Science* **373**, 61–65 (2021).
5. Mohammadi, P. et al. Biomimetic composites with enhanced toughening using silk inspired triblock proteins and aligned nanocellulose reinforcements. *Sci. Adv.* 1–12 https://doi.org/10.1126/sciadv.aaw2541 (2019).
6. Mohammadi, P. et al. Bioinspired functionally graded composite assembled using cellulose nanocrystals and genetically engineered proteins with controlled biomineralization. *Adv. Mater.* **33**, 2102658 (2021).
7. Ling, S., Kaplan, D. L. & Buehler, M. J. Nanofibrils in nature and materials engineering. *Nat. Rev. Mater.* **3**, 1–15 (2018).
8. Barthelat, F., Yin, Z. & Buehler, M. J. Structure and mechanics of interfaces in biological materials. *Nat. Rev. Mater.* **1**, 16007 (2016).
9. Miserez, A., Yu, J. & Mohammadi, P. Protein-based biological materials: molecular design and artificial production. *Chem. Rev.* **123**, 2049–2111 (2023).
10. Laakko, T. et al. Accelerated engineering of ELP-based materials through hybrid biomimetic-de novo predictive molecular design. *Adv. Mater.* 2312299 https://doi.org/10.1002/adma.202312299 (2024).
11. Patravale, V. B. & Mandawgade, S. D. Novel cosmetic delivery systems: an application update. *Int. J. Cosmet. Sci.* **30**, 19–33 (2008).
12. Garti, N. & Bisperink, C. Double emulsions: progress and applications. *Curr. Opin. Colloid Interface Sci.* **3**, 657–667 (1998).
13. Lei, Y. et al. Injectable hydrogel microspheres with self-renewable hydration layers alleviate osteoarthritis. *Sci. Adv.* **8**, eabl6449 (2022).
14. Folkmann, A. W., Putnam, A., Lee, C. F. & Seydoux, G. Regulation of biomolecular condensates by interfacial protein clusters. *Science (1979)* **373**, 1218–1224 (2021).
15. Yucel, T., Lovett, M. L. & Kaplan, D. L. Silk-based biomaterials for sustained drug delivery. *J. Control. Release* **190**, 381–397 (2014).
16. Li, W. et al. High drug-loaded microspheres enabled by controlled in-droplet precipitation promote functional recovery after spinal cord injury. *Nat. Commun.* **13**, 1–16 (2022).
17. Lin, X., Cai, L., Cao, X. & Zhao, Y. Stimuli-responsive silk fibroin for on-demand drug delivery. *Smart Med.* **2**, e20220019 (2023).
18. Wang, L. et al. Advances in the delivery systems for oral antibiotics. *Biomed. Technol.* **2**, 49–57 (2023).
19. Furtado, M., Chen, L., Chen, Z., Chen, A. & Cui, W. Development of fish collagen in tissue regeneration and drug delivery. *Eng. Regener.* **3**, 217–231 (2022).
20. Pylkkänen, R. et al. β−1,3-Glucan synthesis, novel supramolecular self-assembly, characterization and application. *Nanoscale* https://doi.org/10.1039/D2NR02731C (2022).
21. Shi, S. et al. Recent progress in protective membranes fabricated via electrospinning: advanced materials, biomimetic structures, and functional applications. *Adv. Mater.* **34**, 2107938 (2022).
22. Liu, S. et al. Advancements in electrospun nanofibrous membranes for improved waterproofing and breathability. *Macromol. Mater Eng.* 2300312 https://doi.org/10.1002/mame.202300312 (2023).
23. Zhang, Z., Ji, D., He, H. & Ramakrishna, S. Electrospun ultrafine fibers for advanced face masks. *Mater. Sci. Eng. R Rep.* **143**, 100594 (2021).
24. Ullah, S. et al. Reusability comparison of melt-blown vs nanofiber face mask filters for use in the coronavirus pandemic. *ACS Appl. Nano Mater.* **3**, 7231–7241 (2020).
25. Halim, N. S. A. et al. Recent development on electrospun nanofiber membrane for produced water treatment: a review. *J. Environ. Chem. Eng.* **9**, 104613 (2021).
26. Lu, T. et al. Multistructured electrospun nanofibers for air filtration: a review. *ACS Appl. Mater. Interf.* **13**, 23293–23313 (2021).
27. Russo, F., Castro-Muñoz, R., Santoro, S., Galiano, F. & Figoli, A. A review on electrospun membranes for potential air filtration application. *J. Environ. Chem. Eng.* **10**, 108452 (2022).
28. Shi, J. et al. Smart textile-integrated microelectronic systems for wearable applications. *Adv. Mater.* **32**, 1901958 (2020).
29. Zhao, L. et al. Electrospun functional materials toward food packaging applications: a review. *Nanomaterials* **10**, 150 (2020).

30. Ansarifar, E. & Moradinezhad, F. Encapsulation of thyme essential oil using electrospun zein fiber for strawberry preservation. *Chem. Biol. Technol. Agricult.* **9**, 2 (2022).
31. Min, T. et al. Electrospun functional polymeric nanofibers for active food packaging: a review. *Food Chem.* **391**, 133239 (2022).
32. Asai, H. Actuators with nanofiber mat electrodes: effect of electrode preparation method on actuator performance. *Polymer J.* **53**, 1083–1091 (2021).
33. Xu, Y. et al. ECM-inspired micro/nanofibers for modulating cell function and tissue generation. *Sci. Adv.* **6**, https://doi.org/10.1126/sciadv.abc20 (2020).
34. McKee, M. G., Layman, J. M., Cashion, M. P. & Long, T. E. Phospholipid nonwoven electrospun membranes. *Science (1979)* **311**, 353–355 (2006).
35. Wang, Y., Yokota, T. & Someya, T. Electrospun nanofiber-based soft electronics. *NPG Asia Mater.* **13**, 1–22 (2021).
36. Memic, A. et al. Latest progress in electrospun nanofibers for wound healing applications. *ACS Appl. Bio Mater.* **2**, 952–969 (2019).
37. Cao, X., Sun, L., Luo, Z., Lin, X. & Zhao, Y. Aquaculture derived hybrid skin patches for wound healing. *Eng. Regener.* **4**, 28–35 (2023).
38. Shan, J., Che, J., Song, C. & Zhao, Y. Emerging antibacterial nanozymes for wound healing. *Smart Med.* **2**, e20220025 (2023).
39. Fu, X. et al. Oxygen atom-concentrating short fibrous sponge regulates cellular respiration for wound healing. *Adv. Fiber Mater.* **5**, 1773–1787 (2023).
40. Fu, X. et al. Living electrospun short fibrous sponge via engineered nanofat for wound healing. *Adv. Fiber Mater.* **5**, 979–993 (2023).
41. Wang, J. & Windbergs, M. Functional electrospun fibers for the treatment of human skin wounds. *Eur. J. Pharm. Biopharm.* **119**, 283–299 (2017).
42. Zeng, W. et al. Electrospun polycaprolactone nanofibrous membranes loaded with baicalin for antibacterial wound dressing. *Sci. Rep.* **12**, 1–11 (2022).
43. Krysiak, Z. J. & Stachewicz, U. Electrospun fibers as carriers for topical drug delivery and release in skin bandages and patches for atopic dermatitis treatment. *Wiley Interdisciplinary Rev. Nanomed. Nanobiotechnol.* **15**, e1829 (2023).
44. Tahir, U., Shim, Y. B., Kamran, M. A., Kim, D.-I. & Jeong, M. Y. Nanofabrication techniques: challenges and future prospects. *J. Nanosci. Nanotechnol.* **21**, 4981–5013 (2021).
45. Harinarayana, V. & Shin, Y. C. Two-photon lithography for three-dimensional fabrication in micro/nanoscale regime: a comprehensive review. *Opt. Laser Technol.* **142**, 107180 (2021).
46. Sysova, O. et al. Chitosan as a water-developable 193 nm photoresist for green photolithography. *ACS Appl. Polym. Mater.* **4**, 4508–4519 (2022).
47. Wang, Z. et al. Water developable non-chemically amplified photoresist for electron beam and extreme ultraviolet lithography. *J. Micro/Nanopattern. Mater. Metrol.* **21**, 041403 (2022).
48. Paik, S. et al. Near-field sub-diffraction photolithography with an elastomeric photomask. *Nat. Commun.* **11**, 1–13 (2020).
49. Samal, P. et al. Polystyrene pocket lithography: sculpting plastic with light. *Adv. Mater.* **34**, 2200687 (2022).
50. Li, C., Ouyang, L., Armstrong, J. P. K. & Stevens, M. M. Advances in the fabrication of biomaterials for gradient tissue engineering. *Trends Biotechnol.* **39**, 150–164 (2021).
51. Coelho, S., Baek, J., Walsh, J., Justin Gooding, J. & Gaus, K. Direct-laser writing for subnanometer focusing and single-molecule imaging. *Nat. Commun.* **13**, 1–8 (2022).
52. Wang, H. et al. Two-photon polymerization lithography for optics and photonics: fundamentals, materials, technologies, and applications. *Adv. Funct. Mater.* **33**, 2214211 (2023).
53. Lemma, E. D., Spagnolo, B., De Vittorio, M. & Pisanello, F. Studying cell mechanobiology in 3D: the two-photon lithography approach. *Trends Biotechnol.* **37**, 358–372 (2019).
54. Saha, S. K. et al. Scalable submicrometer additive manufacturing. *Science (1979)* **366**, 105–109 (2019).
55. Yasa, I. C., Ceylan, H., Bozuyuk, U., Wild, A. M. & Sitti, M. Elucidating the interaction dynamics between microswimmer body and immune system for medical microrobots. *Sci. Robot* **5**, eaaz3867 (2020).
56. Schindelin, J. et al. Fiji: an open-source platform for biological-image analysis. *Nat. Methods* **9**, 676–682 (2012).
57. Ago, M. et al. High-throughput synthesis of lignin particles (~ 30 nm to~ 2 μm) via aerosol flow reactor: Size fractionation and utilization in Pickering emulsions. *ACS Appl. Mater. Interfaces* **8**, 23302–23310 (2016).

Acknowledgements

This work was supported by the Academy of Finland Grant No. 348628, Jenny and Antti Wihuri Foundation (Center for Young Synbio Scientists), the Academy of Finland Center of Excellence Program (2022–2029) in Life-Inspired Hybrid Materials (LIBER) Grant No. 346106, as well as internal funding from the VTT Technical Research Center of Finland. We acknowledge the provision of facilities and technical support by Aalto University at the OtaNano Nanomicroscopy Center (Aalto-NMC).

Author contributions

Zhuoran Geng: investigation, validation of 3D litography; Timo Laakko: investigation, validation of AIMS predicted hybrid biomimetic-de novo design ELP variants. Ari Hokkanen: investigation, validation of the laser lithography and surface micro-patterning; Caj Södergård: conceptualization; Ilari Maasilta: conceptualization and funding; Pezhman Mohammadi: conceptualization, investigation, validation of drug encapsulation as well as supervision of the project and funding. All authors contributed equally to analysis, discussion of the data, writing, editing, revising, and approving the final version of the manuscript.

Competing interests

The authors declare no competing interests.

Additional information

Correspondence and requests for materials should be addressed to Pezhman Mohammadi.

Peer review information *Communications Materials* thanks the anonymous reviewers for their contribution to the peer review of this work. Primary Handling Editors: Jet-Sing Lee.